The rate of stellar encounters along a migrating orbit of the Sun

Martinez Barbosa, C.A.; Jilkova, L.; Portegies Zwart, S.F.; Brown, A.G.A.

Monthly Notices
of the
ROYAL ASTRONOMICAL SOCIETY

MNRAS **464,** 2290–2300 (2017)
Advance Access publication 2016 October 5

doi:10.1093/mnras/stw2507

The rate of stellar encounters along a migrating orbit of the Sun

C. A. Martínez-Barbosa,★† L. Jílková,★† S. Portegies Zwart★ and A. G. A. Brown
Leiden Observatory, University of Leiden, PB 9513, Leiden NL-2300 RA, the Netherlands

Accepted 2016 October 4. Received 2016 September 28; in original form 2016 May 5

ABSTRACT

The frequency of Galactic stellar encounters the Solar system experienced depends on the local density and velocity dispersion along the orbit of the Sun in the Milky Way galaxy. We aim at determining the effect of the radial migration of the solar orbit on the rate of stellar encounters. As a first step, we integrate the orbit of the Sun backwards in time in an analytical potential of the Milky Way. We use the present-day phase-space coordinates of the Sun, according to the measured uncertainties. The resulting orbits are inserted in an *N*-body simulation of the Galaxy, where the stellar velocity dispersion is calculated at each position along the orbit of the Sun. We compute the rate of Galactic stellar encounters by employing three different solar orbits – migrating from the inner disc, without any substantial migration and migrating from the outer disc. We find that the rate for encounters within 4×10^5 au from the Sun is about 21, 39 and 63 Myr^{-1}, respectively. The stronger encounters establish the outer limit of the so-called parking zone, which is the region in the plane of the orbital eccentricities and semi-major axes where the planetesimals of the Solar system have been perturbed only by interactions with stars belonging to the Sun's birth cluster. We estimate the outer edge of the parking zone at semimajor axes of 250–1300 au (the outwards and inwards migrating orbits reaching the smallest and largest values, respectively), which is one order of magnitude smaller than the determination made by Portegies Zwart & Jílková. We further discuss the effect of stellar encounters on the stability of the hypothetical Planet 9.

Key words: Sun: general – planets and satellites: dynamical evolution and stability – solar neighbourhood.

1 INTRODUCTION

To explain the constant rate of observed new long-period comets, Oort (1950) suggested that more than 10^{11} icy bodies orbit the Sun with aphelia of 5–15 $\times$ 10^4 au, and isotropically distributed inclinations of their orbital planes. The comets are delivered to the inner Solar system from the cloud due to perturbation by the Galactic tide and passing stars (see for example, Rickman 2014 or Dones et al. 2015 for summaries), and the interstellar medium such as the giant molecular clouds (e.g. Hut & Tremaine 1985; Brunini & Fernandez 1996; Jakubík & Neslušan 2009, 2008).

The Galactic tide has a stronger overall effect when averaged over long time-scales (for example, Heisler & Tremaine 1986). The effect of the encounters is stochastic and helps to keep the Oort cloud isotropic (e.g. Kaib, Roškar & Quinn 2011, and references therein). The two mechanisms act together and combine in a non-linear way (Rickman et al. 2008; Fouchard et al. 2011).

The trajectory of the Sun in the Galaxy determines the intensity of the gravitational tides the Solar system has been exposed to, as well as the number of stars around the Sun that could pass close enough to perturb the Oort cloud. Kaib et al. (2011) investigated the effect of encounters with the field stars and that of the Galactic tides on the Oort cloud, considering the so-called radial migration effect on the orbit of the Sun (see e.g. Sellwood & Binney 2002; Roškar et al. 2008; Minchev & Famaey 2010; Martínez-Barbosa, Brown & Portegies Zwart 2015, for a more detailed description). They simulated the Oort cloud around the Sun, adopting possible solar orbits from the simulation of a Milky Way-like galaxy of Roškar et al. (2008), including those that experienced no migration and those that experienced strong radial migration (some of their solar analogues get as close as 2 kpc from the Galactic Centre or as far as 13 kpc). Kaib and collaborators found that the present-day structure of the Oort Cloud strongly depends on the Sun's orbital history, in particular, on its minimum past Galactocentric distance. The inner edge of the Oort cloud shows a similar dependence (on the orbital history of the Sun) and it is also influenced by the effect of strong encounters between the Sun and other stars.

With the increasing amount of precise astrometric and radial velocity data for the stars in the solar neighbourhood, several studies have focused on the identification of stars that passed close to the

★ E-mail: cmartinez@strw.leidenuniv.nl (CAM-B);
jilkova@strw.leidenuniv.nl (LJ); spz@strw.leidenuniv.nl (SPZ)
† Both authors contributed equally to this work.

Solar system in the recent past, or will pass close by in the future (Bailer-Jones 2015; Dybczyński & Berski 2015; Mamajek et al. 2015). Mamajek et al. (2015) identified the star that is currently known to have made the closest approach to the Sun – the so called Scholz's star that passed the Solar system at $0.25^{+0.11}_{-0.07}$ pc. Additionally, Feng & Bailer-Jones (2015) studied the effect of recent and future stellar encounters on the flux of the long-period comets. They carried out simulations of the Oort cloud, considering perturbations by the identified encounters and a constant Galactic field at the current solar Galactocentric radius, and kept track of the flux of long-period comets injected into the inner Solar system as a consequence of the encounters. Unlike Kaib et al. (2011), Feng & Bailer-Jones (2015) focused only on the effect of the actually observed perturbers. They conclude that past encounters in their sample explain about 5 per cent of the currently observed long-period comets and they suggest that the Solar system experienced more strong, as yet unidentified, encounters.

Portegies Zwart & Jílková (2015) discuss the effect of the stellar encounter history on the structure of the system of planetesimals surrounding the Sun. They considered encounters with stars in the Sun's birth cluster (early on in the history of the Sun) and encounters with field stars that occur as the Sun orbits in the Galaxy. The encounters with the field stars set the outer edge of the so-called Parking zone of the Solar system (Portegies Zwart & Jílková 2015). The parking zone is defined as a region in the plane of semimajor axis and eccentricity of objects orbiting the Sun that have been perturbed by the parental star cluster but not by the planets or the Galactic perturbations. The orbits located in the parking zone maintain a record of the interaction of the Solar system with stars belonging to the Sun's birth cluster. Therefore, these orbits carry information that can constrain the natal environment of the Sun. Recently, Jílková et al. (2015) argued that a population of observed planetesimals with semimajor axes >150 au and perihelia >30 au would live in the parking zone of the Solar system. They also found that such a population might have been captured from a debris disc of another star during a close flyby that happened in the Sun's birth cluster.

The outer edge of the parking zone is defined by the strongest encounter the Solar system experienced after it left its birth cluster. The strength of the encounter is measured by the perturbation of semimajor axes and eccentricity of the bodies in their orbit around the Sun. Portegies Zwart & Jílková (2015) used the impulse approximation (Rickman 1976) to estimate the effect and defined the outer edge of the Solar system's parking zone as corresponding to the perturbation caused by the Scholz's star (Mamajek et al. 2015). However, stronger encounters might have happened in the past, as the Sun orbited in the Galactic disc. These encounters would alter the outer edge of the Solar system's parking zone moving it closer to the Sun. The perturbation strength of the stellar encounters depends on the characteristics of the close encounters with field stars – the mass of the other star, its closest approach and relative velocity. Similar to Scholz's star, the parameters of some of the recent close encounters can be derived from the observed data (for example, Dybczyński & Berski 2015; Feng & Bailer-Jones 2015).

Estimates of the number and strength of past encounters are difficult to make because of the large uncertainties in the Galactic environment where the Sun has been moving since it left its birth cluster. These uncertainties are due to the unknown evolution of the Galactic potential (leading to uncertainties in the Sun's past orbit), which is, in turn, related to the unknown (population dependent) density and velocity dispersion of the Milky Way stars along the Sun's orbit. García-Sánchez et al. (2001) studied the recent encounter history of the Sun by integrating its orbit in an analytical Milky Way potential together with 595 stars from the *Hipparcos* catalogue in order to identify recent and near future encounters. In addition, they estimated the encounter frequency for the Sun in its present environment by considering the velocity dispersions and number densities of different types of stars. Rickman et al. (2008) simulated the stellar encounters by assuming random encounter times (for a fixed number of encounters) over 5 billion yr and using velocity dispersions for 13 different types of stars (different masses), with relative encounter frequencies for these types taken from García-Sánchez et al. (2001). An alternative approach based on a numerical model of the Milky Way was taken by Kaib et al. (2011). The orbits of solar analogues in this model were extracted from a simulation of a Milky Way-like galaxy and then the encounters were simulated by tracking the stellar number density and velocity dispersion along the orbit and then generating random encounters by starting stars at random orientations 1 pc from the Sun. The encounter velocities were generated using the recipe by Rickman et al. (2008).

In this paper, we aim to improve the determination of the outer edge of the Solar system's parking zone by determining the number of stellar encounters experienced by the Sun along its orbit. We compute the number of encounters by employing the largest Milky Way simulation to date, which contains 51 billion particles, divided over a central bulge, a disc and a dark matter halo (Bédorf et al. 2014). This Galaxy model is used to estimate the velocity dispersion of the stars encountered by the Sun along its orbit. To achieve this, we integrate the Sun's orbit back in time using an analytical potential for the Milky Way. The orbit of the Sun is then inserted in a snapshot of the particle simulation and the velocity dispersion of the disc stars is estimated at each position. We employ three different orbits of the Sun (no radial migration, migration inwards, migration outwards) and use the resulting estimates of the encounter frequencies along each of these orbits to discuss the implications for the location of the outer edge of the Solar system's parking zone. We also discuss the effect of such encounters on the stability of the orbit of the so-called Planet 9 (P9). The presence of this object was predicted by Batygin & Brown (2016) in the outer Solar system to explain the clustering of the orbital elements of the distant Kuiper Belt Objects (KBOs). According to the updated simulations of Brown & Batygin (2016), P9 has a mass of 5–20 $M_{\oplus}$; an eccentricity of ∼0.2–0.8, semimajor axis of ∼500–1050 au and perihelion distance of ∼150–350 au.

This paper is organized as follows: in Section 2, we explain the Galaxy model and we show three possible orbital histories of the Sun. In Section 3, we determine the number of encounters along each of these solar orbits. From this estimate, we generate a set of stellar encounters with random mass, encounter distance and velocity. In Section 4, we find the stellar encounters that produce the strongest perturbation of objects orbiting the Sun. These encounters are used to estimate the outer edge of the Solar system's parking zone. In Section 5, we discuss the effects of such encounters on the stability of the orbit of P9. We also mention the limitations of our computations and the improvements that could be made in future studies. In Section 6, we summarize.

2 GALAXY MODEL AND POSSIBLE ORBITAL HISTORIES OF THE SUN

We use an analytical potential to model the Milky Way. This potential is used to calculate possible solar orbits. The Galactic potential contains axisymmetric and non-axisymmetric components. The axisymmetric part contains a bulge, disc and dark matter halo. The

Table 1. Modeling parameters of the Milky Way.

Axisymmetric component		
Mass of the bulge (M_b)	1.41×10^{10} M$_\odot$	
Scalelength bulge (b_1)	0.3873 kpc	
Disc mass (M_d)	8.56×10^{10} M$_\odot$	
Scalelength 1 disc (a_2)	5.31 kpc	(1)
Scalelength 2 disc (b_2)	0.25 kpc	
Halo mass (M_h)	1.07×10^{11} M$_\odot$	
Scalelength halo (a_3)	12 kpc	
Central bar		
Pattern speed (Ω_{bar})	55 km s^{-1} kpc^{-1}	(2)
Mass (M_{bar})	9.8×10^9 M$_\odot$	(4)
Semimajor axis (a)	3.1 kpc	(5)
Axis ratio (b/a)	0.37	(5)
Vertical axis (c)	1 kpc	(6)
Present-day orientation	20°	(3)
Spiral arms		
Pattern speed (Ω_{sp})	25 km s^{-1} kpc^{-1}	(2)
Number of spiral arms (m)	2	(7)
Amplitude (A_{sp})	3.9×10^7 M$_\odot$ kpc^{-3}	(4)
Pitch angle (i)	15.5	(4)
Scalelength (R_Σ)	2.6 kpc	(7)
Scaleheight (H)	0.3 kpc	(7)
Present-day orientation	20°	(5)

References: (1) Allen & Santillán (1991); (2) Gerhard (2011); (3) Romero-Gómez et al. (2011); (4) Jílková et al. (2012); (5) Martínez-Barbosa et al. (2015); (6) Monari et al. (2014); (7) Drimmel (2000); (8) Jurić et al. (2008).

non-axisymmetric part contains a bar and spiral arms, which rotate as rigid bodies with different pattern speeds.

Given the configuration of the Galactic potential, we define three coordinate systems.

(i) An inertial system that is fixed at the centre of the Galaxy, whose coordinates are denoted by $\boldsymbol{x} = (x, y, z)$.

(ii) A system that corotates with the bar, whose coordinates are denoted by $\boldsymbol{x}_{\rm rot} = (x_{\rm rot}, y_{\rm rot}, z_{\rm rot})$. In this frame, the bar is located along the x-axis. The initial orientation and velocity of this rotating system correspond to the present-day orientation and pattern speed of the bar, respectively (see Table 1).

(iii) A system that co-rotates with the spiral arms, whose coordinates are denoted by $\boldsymbol{x}_{\rm rot_l} = (x_{\rm rot_l}, y_{\rm rot_l}, z_{\rm rot_l})$. The initial orientation and velocity of this rotating system correspond to the present-day orientation and pattern speed of the spiral arms (see Table 1).

The reference systems explained above are shown in Fig. 1 and we use them to compute the components of the Galactic potential. The axisymmetric potential is calculated in the inertial frame, while the potential of the bar and spiral arms are calculated in their respective co-rotating frames. We, however, compute the orbit of the Sun in the inertial system. Therefore, we use coordinate transformations to go from $\boldsymbol{x}_{\rm rot}$ or $\boldsymbol{x}_{\rm rot_l}$ to $\boldsymbol{x}$.

Hereafter, the coordinates r and R represent the spherical and cylindrical radii. φ is the angle measured from the x-axis and in the direction opposite to the Galactic rotation (i.e. counter-clockwise). z is the vertical component, perpendicular to the plane of the Galactic diskdisc.

In Sections 2.1–2.3, we give a detailed description of the axisymmetric and non-axisymmetric components of the Galactic potential.

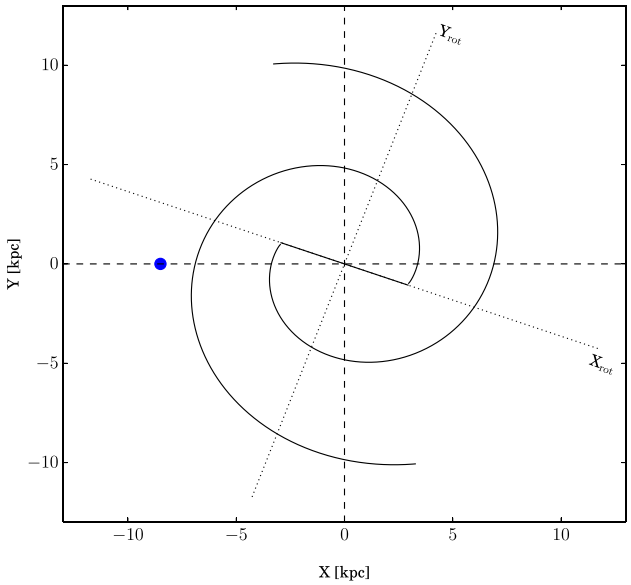

Figure 1. Configuration of the bar and spiral arms of the Galaxy at the present time. The blue circle marks the current position of the Sun measured in an inertial system that is fixed at the centre of the Galaxy. The axes $X_{\rm rot}$ and $Y_{\rm rot}$ correspond to a system that co-rotates with the bar. Note that the spiral arms start at the edges of the bar, therefore the coordinates $(X_{\rm rot_l}, Y_{\rm rot_l})$ and $(X_{\rm rot}, Y_{\rm rot})$ overlap at the present time.

2.1 Axisymmetric component

As mentioned before, the axisymmetric component of the Galaxy consists of a bulge, disc and a dark matter halo. We model the bulge of the Milky Way as a Plummer potential (Plummer 1911):

$$\Phi_{\rm bulge} = -\frac{GM_{\rm b}}{\sqrt{r^2 + b_1^2}}\,, \tag{1}$$

where G corresponds to the gravitational constant, $M_{\rm b}$ is the mass of the bulge and b_1 is its corresponding scalelength.

The disc of the Milky Way was modelled by using a Miyamoto–Nagai potential (Miyamoto & Nagai 1975), which is described by the expression:

$$\Phi_{\rm disc} = -\frac{GM_{\rm d}}{\sqrt{R^2 + \left(a_2 + \sqrt{z^2 + b_2^2}\right)^2}}\,. \tag{2}$$

Here $M_{\rm d}$ corresponds to the mass of the disc. The parameters a_2 and b_2 are constants that modulate its shape. In particular, when $a_2 = 0$, equation (2) represents a spherical distribution of mass. In the case where $b_2 = 0$, equation (2) corresponds to the potential of a completely flattened disc.

Finally, we model the dark matter halo by means of a logarithmic potential of the form:

$$\Phi_{\rm halo} = -\frac{GM(r)}{r} - \frac{GM_{\rm h}}{1.02a_3}\left[-\frac{1.02}{1+\Re^{1.02}} + \ln\left(1+\Re^{1.02}\right)\right]_r^{100}\,, \tag{3}$$

where

$$M(r) = \frac{M_{\rm h}\Re^{2.02}}{1+\Re^{1.02}} \quad \text{and}$$

$$\Re = \frac{r}{a_3}\,.$$

The parameters in equations (1)–(3) were taken from Allen & Santillán (1991) and they are listed in Table 1. Although the model introduced by Allen & Santillán (1991) does not precisely represent the current estimates of the mass distribution in the Galaxy, this model has been widely used in studies of orbits of open clusters (Allen, Moreno & Pichardo 2006; Bellini et al. 2010) and in studies of moving groups in the solar neighbourhood (Antoja et al. 2009, 2011). Moreover, Jílková et al. (2012) did not find substantial differences in the orbit of an open cluster when the axisymmetric component is described by a different, more up-to-date model. Therefore, we do not expect that the modelling of the axisymmetric component of the Galaxy influences the results obtained in this study.

2.2 Galactic bar

We model the bar of the Galaxy with a three-dimensional Ferrers potential (Ferrers 1877), which is represented by the following density:

$$\rho_{\rm bar} = \begin{cases} \rho_0 \left(1 - n^2\right)^k & n < 1 \\ 0 & n \geq 1 \end{cases} . \tag{4}$$

The quantity n determines the shape of the bar, which is given by the equation: $n^2 = x_{\rm rot}^2/a^2 + y_{\rm rot}^2/b^2 + z_{\rm rot}^2/c^2$, where the parameters a, b and c are the semimajor, semiminor and vertical axes of the bar, respectively. The term ρ_0 in equation (4) represents the central density of the bar and k its concentration. Following Romero-Gómez et al. (2011), we chose $k = 1$.

The parameters that describe the bar such as its pattern speed, mass, orientation and axes are currently under debate (for a complete discussion, see e.g. Martínez-Barbosa et al. 2015). Hence, we used values that are within the ranges reported in the literature. These values are listed in Table 1.

2.3 Spiral arms

The spiral arms are usually represented as periodic perturbations of the axisymmetric potential. We use the prescription given by Cox & Gómez (2002), which models such perturbations in the three-dimensional space. The potential of the spiral arms is given by the following expression:

$$\Phi_{\rm sp} = -4\pi G H A_{\rm sp} \exp\left(-\frac{r_{\rm rot_1}}{R_\Sigma}\right) \sum_n \left(\frac{C_n}{K_n D_n}\right) \times \cos(n\gamma) \left[\operatorname{sech}\left(\frac{K_n z_{\rm rot_1}}{\beta_n}\right)\right]^{\beta_n}, \tag{5}$$

where $r_{\rm rot_1}$ is the distance of the star from the Galactic Centre, measured in the frame co-rotating with the spirals arms. The value H is the scaleheight, $A_{\rm sp}$ is the amplitude of the spiral arms and R_Σ is the scalelength of the drop-off in density amplitude of the arms. We use $n = 1$ term only, with $C_1 = 8/3\pi$ and the parameters K_1, D_1 and β_1 given by

$$K_1 = \frac{m}{r_{\rm rot_1} \sin i},$$

$$\beta_1 = K_1 H (1 + 0.4 K_1 H),$$

$$D_1 = \frac{1 + K_1 H + 0.3 (K_1 H)^2}{1 + 0.3 K_1 H},$$

where m and i correspond to the number of arms and pitch angle of the spiral structure, respectively.

Finally, the term γ in equation (5) represents the shape of the spiral structure, which is described by the expression:

$$\gamma = m \left[\varphi - \frac{\ln(r_{\rm rot1}/r_0)}{\tan i}\right] .$$

Here r_0 is a parameter that determines the scalelength of the spiral arms. Following Jílková et al. (2012), $r_0 = 5.6$ kpc.

As for the bar, the parameters that describe the spiral structure of the Galaxy are rather uncertain (See e.g. Jílková et al. 2012; Martínez-Barbosa et al. 2015). Therefore, we chose the values that are consistent with the current determination of the spiral structure. These values are listed in Table 1.

2.4 Solar orbits

We calculate the orbit of the Sun backwards in time using the analytical Galaxy model described previously. In this calculation, we account for the uncertainty in the present-day Galactocentric phase-space coordinates of the Sun. We employ the same methodology as used by Martínez-Barbosa et al. (2015) for this purpose.[1] Thus, we select a sample of 5000 random positions and velocities from a normal distribution centred at the current phase-space coordinates of the Sun. The normal distribution is then centred at $(r_\odot, v_\odot)$ with standard deviations (σ) corresponding to the uncertainties in these coordinates. In an inertial frame that is fixed at the centre of the Galaxy, the present-day location of the Sun is (see Fig. 1):

$$r_\odot = (-8.5, 0, 0.02)\ \text{kpc} \quad \text{and}$$
$$\sigma_r = (0.5, 0, 0.005)\ \text{kpc},$$

where the position of the Sun in the plane is given by $\mathrm{R}_\odot = 8.5$ kpc.

The present-day velocity of the Sun is

$$v_\odot = (11.1, 12.4 + v_{\rm LSR}, 7.25)\ \text{km s}^{-1} \quad \text{and}$$
$$\sigma_{\rm v} = (1.2, 2.1, 0.6)\ \text{km s}^{-1},$$

where $v_\odot$ and $\sigma_{\rm v}$ were taken from Schönrich, Binney & Dehnen (2010) and $v_{\rm LSR}$ corresponds to the velocity in the Local Standard of Rest (LSR). According to the Milky Way model parameters listed in Table 1, $v_{\rm LSR} = 226\ \text{km s}^{-1}$.

We integrate the orbit of the Sun backwards in time using each of the 5000 positions and velocities as initial phase-space coordinates. The solar orbits were computed during 4.6 Gyr by using a sixth-order integrator called Rotating BRIDGE (Martínez-Barbosa et al. 2015, Pelupessy et al., in preparation). This integrator is implemented in the AMUSE framework (Pelupessy et al. 2013; Portegies Zwart et al. 2013).

At the end of the calculation, we obtain a collection of solar orbits, from which we chose three. These orbits are shown in Fig. 2 and they represent different orbital histories of the Sun through the Galaxy. The blue orbit, for instance, shows that the Sun might have been born at ∼11 kpc from the Galactic Centre, suggesting migration from outer regions of the Galactic disc to $\mathrm{R}_\odot$. Martínez-Barbosa et al. (2015) argued that such a migration could only have happened if the Sun was influenced by the overlapping of the co-rotation resonance of the spiral arms with the outer Lindblad resonance of the bar. On the other hand, the violet orbit shows an example where

[1] Unlike Martínez-Barbosa et al. (2015), we use a three-dimensional model for the Galaxy in this study; see Section 2.3.

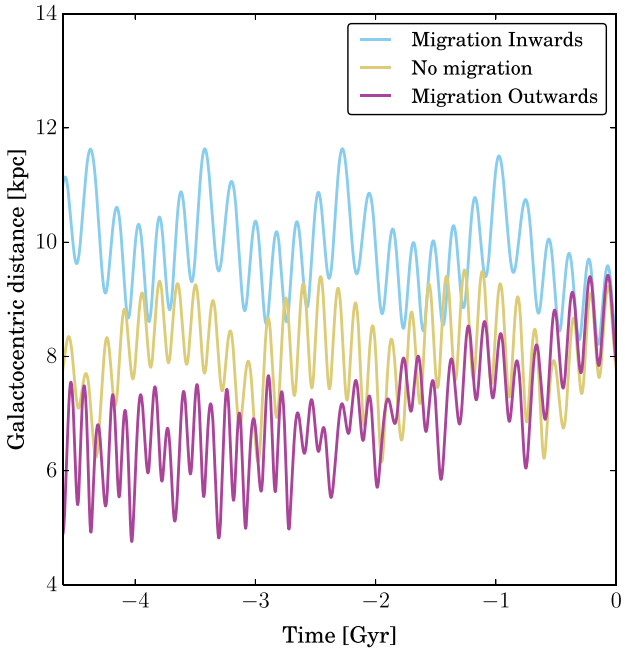

Figure 2. Possible trajectories of the Sun under the Galactic parameters listed in Table 1. $t = 0$ Gyr represents the current time.

the Sun migrated from inner parts of the disc to $R_\odot$, in accordance with Wielen, Fuchs & Dettbarn (1996) and Minchev, Chiappini & Martig (2013). The yellow orbit represents the case where the Sun does not migrate on average.

The stellar encounter rate experienced by the Sun during the last 4.6 Gyr depends on the solar orbit, due to differences in the stellar density and in the local stellar velocity dispersion. Therefore, we compute the number of stellar encounters in each of the orbits shown in Fig. 2. The methodology is described in Section 3.

3 GALACTIC STELLAR ENCOUNTERS

The frequency of stellar passages along the orbit of the Sun, f, can be estimated by the following equation (García-Sánchez et al. 2001):

$$f = \sum_i f_i = \pi D^2 \sum_i n_i v_i. \tag{6}$$

The index i denotes different stellar types according to the classification given in García-Sánchez et al. (2001, table 8). The term D corresponds to the maximum pericentric distance from the Sun where a stellar encounter is considered. We set $D = 4 \times 10^5$ au, because we do not expect farther encounters to substantially perturb the Solar system (see e.g. Rickman et al. 2008; Feng & Bailer-Jones 2014). The quantity n_i in equation (6) corresponds to the number density of each stellar type, along the orbit of the Sun. The term v_i is the velocity of the encounter that is described by the expression:

$$v_i = \left[v_{\odot i}^2 + v_i^2\right]^{1/2}. \tag{7}$$

Here $v_{\odot i}$ corresponds to the Sun's peculiar velocity relative to the star belonging to the ith category (we assume that $v_{\odot i}$ is constant everywhere in the Galaxy). The term ν_i is the velocity dispersion of the given stellar type, along the orbit of the Sun.

We obtain n_i and ν_i by using a similar procedure briefly described in Kaib et al. (2011). In Sections 3.1 and 3.2, we explain this methodology in more detail.

3.1 Estimation of n_i

We obtain the number density of a given stellar type along the orbit of the Sun, n_i, by scaling up or down the number density of that stellar type at the current solar position, $n_{i\odot}$. The number density, n_i, is therefore given by the following expression:

$$n_i = \beta n_{i\odot}. \tag{8}$$

We take the values of $n_{i\odot}$ from (García-Sánchez et al. 2001, table 8). The quantity β is a scaling factor that depends on the location of the Sun in the Galaxy. We compute β by assuming that the number densities have the same spatial distribution through the Galaxy (see e.g. Feng & Bailer-Jones 2014). The scaling factor is therefore equal to:

$$\beta = \frac{\rho}{\rho_\odot}, \tag{9}$$

where ρ is the local stellar mass density along the Sun's orbit and $\rho_\odot$ is the local stellar density at the current Sun's position. We compute ρ and $\rho_\odot$ through the Poisson's equation using the Galaxy potential described in Section 2. In the calculation of the local stellar mass density, we do not include the dark matter halo potential.

3.2 Estimation of ν_i

We obtain the velocity dispersion of a given stellar type along the Sun's orbit, ν_i, by scaling up or down the velocity dispersion of that stellar type at the current position of the Sun, $\nu_{i\odot}$. The velocity dispersion ν_i is described by the following expression:

$$\nu_i = \alpha \nu_{i\odot}. \tag{10}$$

The values of $\nu_{i\odot}$ are taken from García-Sánchez et al. (2001, table 8). The scaling factor α depends on the location of the Sun in the Galaxy and it is given by

$$\alpha = \frac{\nu}{\nu_\odot}, \tag{11}$$

where ν is the total velocity dispersion at a given location along the Sun's orbit and $\nu_\odot$ is the total velocity dispersion at the current position of the Sun. $\nu_\odot$ is the weighted average of the velocity dispersions per stellar type (the weights being equal to $n_{i\odot}$).

We obtain ν by using the largest N-body simulation of the Milky Way, which employs a total number of 51 billion particles (Bédorf et al. 2014). We did not use the Galactic model described in Section 2 given the complexity in the estimate of ν from an analytical Galaxy model. Although the computation of ν by means of a different Galaxy model is not consistent, we note that the simulations of Bédorf et al. (2014) have successfully reproduced the stellar velocity distribution within 500 pc from the Sun (see e.g. fig. 3 in their paper).

We compute ν by using the snapshot of the simulation of Bédorf et al. (2014) corresponding to 5.6 Gyr of evolution. We chose this snapshot because it corresponds well to the current picture of the Milky Way. In this snapshot, we discretize the space in bins of $(\Delta_R, \Delta_\varphi, \Delta_z) = (0.3\,\mathrm{kpc}, 0.26\,\mathrm{rad}, 5\,\mathrm{pc})$, respectively. This choice ensures a robust estimate of ν because of the number of particles located at each bin. The region in the Galaxy where we determine ν is: $0 \leq R \leq 15$ kpc; $0 \leq \varphi \leq 2\pi$ rad and $-200 \leq z \leq 200$ pc.

The velocity dispersion in the jth bin is given by the following expression:

$$\nu_j^2 = \frac{1}{N_j - 1} \sum_{k=1}^{N_j} \left[(v_{\mathrm{R}_{kj}} - \bar{v}_{\mathrm{R}j})^2 + (v_{\varphi kj} - \bar{v}_{\varphi j})^2 + (v_{z_{kj}} - \bar{v}_{zj})^2\right], \tag{12}$$

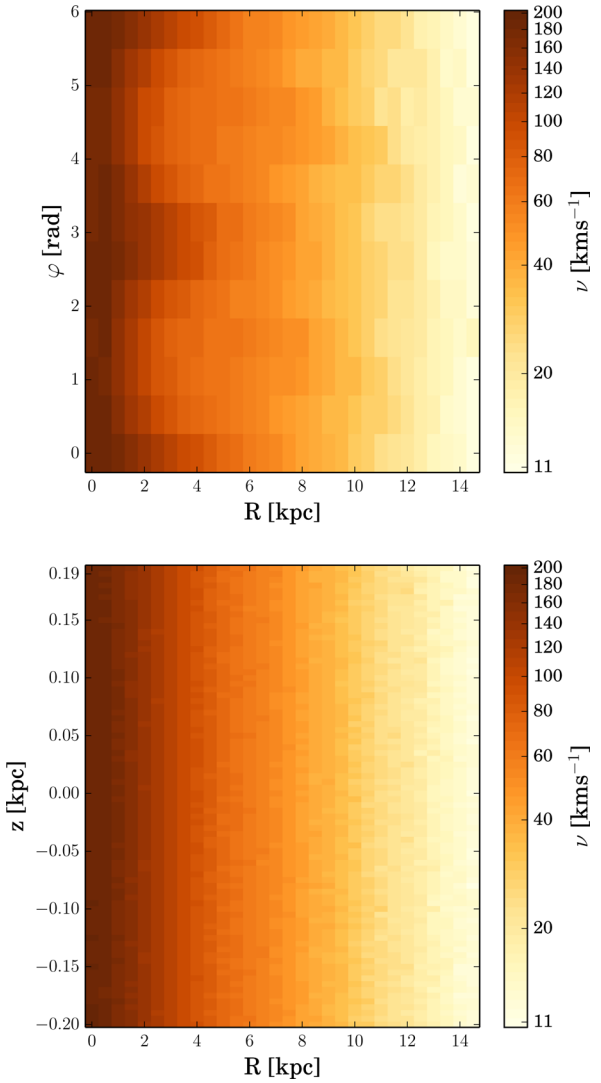

Figure 3. Top: stellar velocity dispersion of the Milky Way as a function of Galactocentric radius and azimuth where $0 \leq z \leq 5$ pc. Bottom: stellar velocity dispersion as a function of Galactocentric radius and vertical distance where $0 \leq \theta \leq \pi/6$ rad.

where $v_{\mathrm{R}_{kj}}$, $v_{\varphi_{kj}}$ and $v_{z_{kj}}$ are the radial, tangential and vertical velocities of the kth star in the jth bin that contains N_j stars. $\bar{v}_{\mathrm{R}\,j}$, $\bar{v}_{\varphi\,j}$ and $\bar{v}_{z\,j}$ are the mean values of the former velocities, respectively.

In Fig. 3, we show ν as a function of the radius and azimuth (top panel) and as a function of the radius and vertical distance (bottom panel). As is expected, the velocity dispersion decreases with radius, due to a reduction of the stellar density in the outer regions of the Galaxy. At the solar position, we observe that $\nu \simeq 40$ km s^{-1}, which is in agreement with measurements of the local velocity dispersion (Nordström et al. 2004; Holmberg, Nordström & Andersen 2009).

The velocity dispersion varies periodically with azimuth, being higher in the inner disc (e.g. top panel, Fig. 3). This variation is a signature of the presence of the bar that extends up to ∼4 kpc from the Galactic Centre. The variation of ν with azimuth is smaller in outer regions of the disc and it is due to the presence of spiral arms. From Fig. 3, we also observe that the variation of the velocity dispersion with the vertical distance z is low compared to the change with radius or azimuth.

Table 2. Mass ranges (M_{enc}) corresponding to the magnitude intervals (M_{V}) of García-Sánchez et al. (2001). The mass intervals for types B0–M5 are based on Pecaut & Mamajek (2013), Pecaut, Mamajek & Bubar (2012) and Mamajek 2016), on Kepler et al. (2007) for white dwarfs (WD) and on Allen (1973) for the giants.

Stellar type	M_{V} (mag)		M_{enc} ($\mathrm{M}_{\odot}$)	
B0	−5.7	−0.2	60	3.4
A0	−0.2	1.3	3.4	2.15
A5	1.3	2.4	2.15	1.67
F0	2.4	3.6	1.67	1.25
F5	3.6	4.0	1.25	1.18
G0	4.0	4.7	1.18	1.02
G5	4.7	5.5	1.02	0.9
K0	5.5	6.4	0.9	0.78
K5	6.4	8.1	0.78	0.64
M0	8.1	9.9	0.64	0.51
M5	9.9	18.0	0.51	0.082
WD[a]	–	–	$\mu = 0.59$,	$\sigma = 0.07$
Giants	–	–	2.5	6.3

Notes.[a]In the case of white dwarfs, the listed numbers μ and σ correspond to the mean and standard deviation of the Gaussian distribution, respectively.

3.3 Total number of encounters along the Sun's orbit

Once n_i and v_i are computed, we can use equation (6) to obtain the frequency of stellar encounters experienced by the Sun along its orbit, f. Given that f is a function of time (note that n_i and v_i change along the orbit), the total number of stellar encounters experienced by the Sun along its orbit is

$$n_{\mathrm{enc}} = \int_{t=0}^{4.5\,\mathrm{Gyr}} f(t)\,\mathrm{d}t. \tag{13}$$

For the solar orbit where the migration is inwards, $n_{\mathrm{enc}} \backsimeq 9.3 \times 10^4$. For the solar orbit with migration outwards, $n_{\mathrm{enc}} \backsimeq 28.2 \times 10^4$. For the orbit with no net migration, $n_{\mathrm{enc}} \backsimeq 17.5 \times 10^4$. We note that this last value is similar to that obtained by Rickman et al. (2008) and Feng & Bailer-Jones (2014) who assumed a non-migrating orbit for the Sun (they found $n_{\mathrm{enc}} = 197\,906$).

For each of the solar orbits shown in Fig. 2, we generate a sample of n_{enc} random stellar encounters. The properties of these encounters – time of occurrence (t_{enc}), mass (M_{enc}), pericentre distance (r_{enc}) and velocity (v_{enc}) – are calculated as explained below.

We randomly draw t_{enc} with a probability that is proportional to the encounter frequency. Once we determine t_{enc}, we proceed to the computation of the mass of the encounters, M_{enc}. This quantity is sampled by using the data listed in García-Sánchez et al. (2001, table 8) that comprise the properties of different stellar types defined by intervals in visible magnitude. First, we determine the ith stellar type of each encounter according to the number density n_i.[2] The mass is determined for each encounter as follows. For stellar types A0–M5, we define mass ranges corresponding to the magnitude intervals based on Pecaut & Mamajek (2013), Pecaut et al. (2012) and Mamajek (2016).[3] We list the magnitude and mass in Table 2. We pick the individual masses from the mass range of the

[2] n_i depends on t_{enc}, since n_i is the stellar density measured along the Sun's orbit (equation 8).

[3] We used data compiled by Mamajek (2016) and publicly available at the web page http://www.pas.rochester.edu/∼emamajek/EEM_dwarf_UBVIJHK_colors_Teff.txt

corresponding stellar type and with distribution given by Kroupa (2001)

$$\frac{\mathrm{d}N}{\mathrm{d}M} \propto \begin{cases} M^{-1.3}, & 0.08 < M \leq 0.5\,\mathrm{M}_\odot, \\ M^{-2.3}, & 0.5 < M < 60\,\mathrm{M}_\odot, \end{cases} \tag{14}$$

where we chose the maximum mass of 60 $\mathrm{M}_\odot$ (the results are not sensitive to the upper limit since the frequency of B0 stars is very low).

For white dwarfs, we assume a Gaussian distribution with the mean of 0.59 $\mathrm{M}_\odot$ and standard deviation of 0.07 $\mathrm{M}_\odot$. We derive these values as means of the four distributions in table 1 of Kepler et al. (2007), weighted by fraction of stars in their sub-samples. Finally, we take the limiting masses for giant stars from Allen (1973, as the masses of G0 and M0 giants) and we assume uniform distribution between 2.5 and 6.3 $\mathrm{M}_\odot$.

We generate the distribution of encounter velocities, $v_{\rm enc}$, by adopting the same methodology as Feng & Bailer-Jones (2014). The procedure is as follows. The magnitude of the encounter velocity in the heliocentric reference frame is

$$v_{\rm enc} = \left[v_{\odot i}^2 + V_i^2 - 2 v_\odot V_i \cos\delta \right]^{1/2}. \tag{15}$$

Here, $v_{\odot i}$ is the solar apex velocity relative to the star of ith category (note that the stellar category was previously chosen from n_i). The term v_i is the velocity of the stellar encounter in the Local Standard of Rest (LSR). δ is the angle between $v_{\odot i}$ and v_i in the LSR.

The velocity of the stellar encounter in the LSR is given by the following equation:

$$V_i = v_i \left[\frac{1}{3} \left(\eta_u^2 + \eta_v^2 + \eta_w^2 \right) \right]^{1/2}, \tag{16}$$

where the quantities η_u, η_v, η_w are random variables that follow a Gaussian distribution with zero mean and unit variance. We obtain the distribution of $v_{\rm enc}$ in the following way: (i) we randomly generate $\cos\delta$ from a uniform distribution in the range $[-1, 1]$. (ii) Adopting $v_{\odot i}$ from (García-Sánchez et al. 2001, table 8) and computing v_i from equation (10), we calculate v_i from equation (16) and $v_{\rm enc}$ using equation (15). (iii) Since we have to account for the fact that the contribution to the encounter flux is proportional to $v_{\rm enc}$, we define a large velocity, $v_{\rm enc} = v_{\odot i} + 3v_i$. (iv) According to the stellar category, we randomly draw a velocity $v_{\rm rand}$ from a uniform distribution over $[0, v_{\rm enc}]$. If $v_{\rm rand} < v_{\rm enc}$, we accept $v_{\rm enc}$ and the generated values of $\cos\delta$, v_i. Otherwise, we reject it and repeat the process until $v_{\rm rand} < v_{\rm enc}$.

Finally, we sample the distances of the stellar encounter, $r_{\rm enc}$, from a distribution function proportional to $r_{\rm enc}$ with an upper limit of 4×10^5 au, in the same fashion as Feng & Bailer-Jones (2014).

For each of the three studied orbits, we calculated and combined 1000 different sets of encounters (realized by different random seeds) following the method described above. In Fig. 4, we show the distributions of the encounters averaged over the total number of sets (1000) in two-dimensional projections of the space of $M_{\rm enc}$, $v_{\rm enc}$ and $r_{\rm enc}$. Note that the distributions do not differ dramatically with migration. As expected from the assumed distributions, most of the encounters are with low-mass stars ($M_{\rm enc} < 1\,\mathrm{M}_\odot$) and velocities of ∼20–100 km s^{-1}.

From the large set of stellar encounters obtained, we can look for those that produce the strongest perturbation in the outer regions of the Solar system. These stellar encounters will set the outer edge of the parking zone. Portegies Zwart & Jílková (2015) used the encounter with Scholz's star to determine the location of the outer edge of the Solar system's parking zone and they found that the effect of this particular encounter has hardly perturbed the Oort cloud down to a distance of 10^5 au. If the Sun experienced stronger stellar encounters, the perturbations might become important at smaller semimajor axes, shifting inwards the outer edge of the parking zone. In the next section, we determine the strongest stellar encounters experienced by the Sun and we make a new estimate of the location of the outer edge of the Solar system's parking zone.

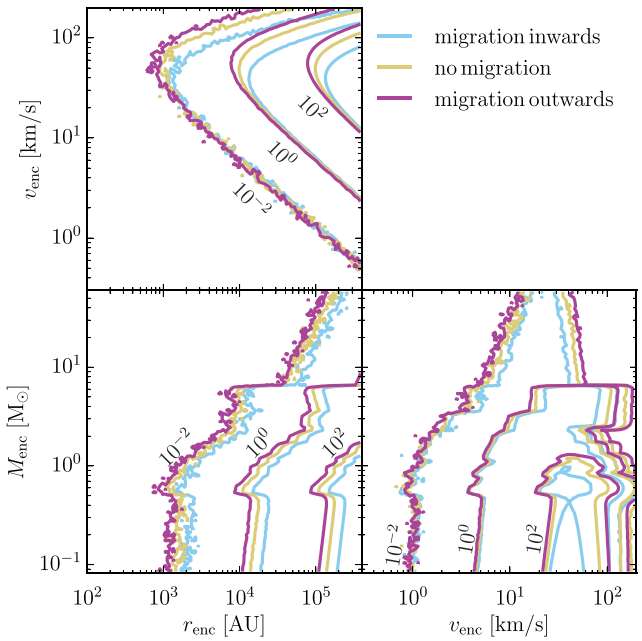

Figure 4. Number of encounters as a function of the mass $M_{\rm enc}$, velocity $v_{\rm enc}$ and pericentre $r_{\rm enc}$ of the encountering star along the three studied orbits. The number of encounters, $n_{\rm enc}$, is averaged over the number of generated sets (1000, see the text). In each subplot, three contours ($n_{\rm enc} = 10^{-2}$, 10^0, 10^2 per bin) of different two-dimensional distributions are shown. The axes are logarithmic and $n_{\rm enc}$ is not normalized by the size of the bin. Hence, the plot serves for the comparison between the three different orbits.

4 THE OUTER LIMIT OF THE PARKING ZONE

We estimate the outer limit of the parking zone using the impulse approximation (Rickman 1976). The impulse approximation assumes that the velocity vector of the perturbing star, $\boldsymbol{v}_{\rm enc}$, and the position vector of the perturbed body orbiting the Sun are constant during the encounter. This corresponds to the assumption that the time-scale of the encounter is much longer than the orbital period of the perturbed body. Following Portegies Zwart & Jílková (2015), we further assume that the point of the closest approach of the star lies on the line joining the Sun and the perturbed body (that is, the velocity of the perturbing star, $\boldsymbol{v}_{\rm enc}$, is perpendicular to the position vector of the perturbed body), which is the geometry resulting in the maximal perturbation. Finally, we assume that the perturbed body is at the aphelion of its orbit where it is moving the slowest.

The impulse gained by a perturbed body moving on an orbit with semimajor axis a and eccentricity e then is

$$\Delta I = \frac{2\mathrm{G}M_{\rm enc}}{v_{\rm enc} r_{\rm enc}} \frac{a(1+e)}{r_{\rm enc} - a(1+e)}. \tag{17}$$

Note that in the case of a distant encounter, when $r_{\rm enc} \gg a(1+e)$, the impulse given in equation (17) at given distance from the Sun is proportional to $M_{\rm enc}/(v_{\rm enc} r_{\rm enc}^2)$. Feng & Bailer-Jones (2015) used this expression as a proxy for the strength of the encounters

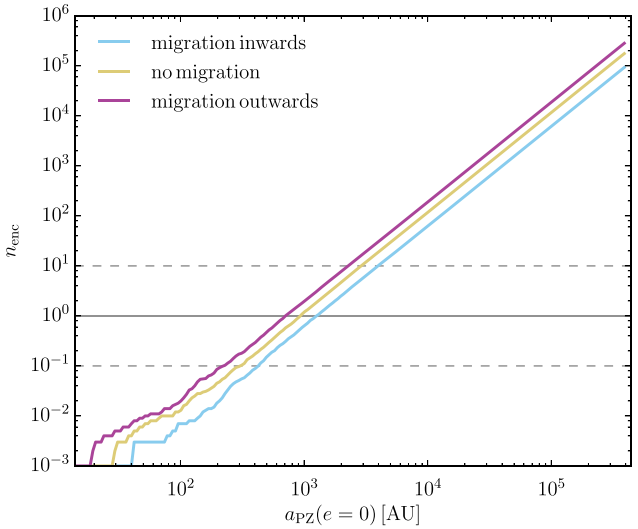

Figure 5. Cumulative distributions of the outer limit of the parking zone for circular orbits $a_{\rm PZ}(e=0)$. The three orbits with different migration are shown. The distributions are derived using 1000 different encounter sets (corresponding to different random seeds) and the number of encounters, $n_{\rm enc}$, is averaged over these number of sets. The maximal value of $a_{\rm PZ}(e=0)$ is given by the upper limit of the encounter pericentre of $D = 4 \times 10^5$ au (Section 3). The maximal value of $n_{\rm enc}$ corresponds to the total number of encounters along the orbits. The horizontal lines indicate $n_{\rm enc} = 0.1$, 1 and 10. Both horizontal and vertical axes are logarithmic.

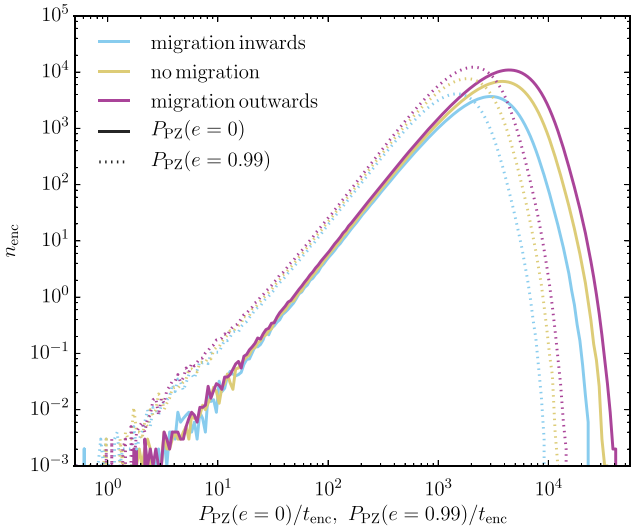

Figure 6. Distributions of the ratio of the period of a circular orbit of semimajor axis $a_{\rm PZ}$ for circular and eccentric ($e = 0.99$) orbits, $P_{\rm PZ}(e=0)$ and $P_{\rm PZ}(e=0.99)$, and the time-scale $t_{\rm enc}$ of the corresponding encounter. The three different orbits are shown by different colours. Full and dotted lines correspond to circular and eccentric orbits, respectively. The distributions are derived for the same combined encounter sets as in Fig. 5. Note that both horizontal and vertical axes are logarithmic.

(as measured by the number of injected long-period comets). We define the outer limit of the parking zone where the perturbation corresponds to the body's velocity at aphelion (Portegies Zwart & Jílková 2015), that is

$$\Delta I = \sqrt{\frac{GM_\odot}{a}\frac{1-e}{1+e}}, \tag{18}$$

where the mass of the Sun is $M_\odot = 1\,{\rm M}_\odot$. From equations (17) and (18), we can find the semimajor axis of the outer limit of the parking zone as a function of eccentricity, $a_{\rm PZ}(e)$.

In Fig. 5, we compare cumulative distributions of the outer limit of the parking zone of a circular orbit, or $a_{\rm PZ}(e=0)$, for encounters along each of the studied orbits. To obtain the distributions, we generated 1000 different sets of encounters for each solar orbit and calculated their $a_{\rm PZ}(e=0)$. The distributions in Fig. 5 are averaged over the number of encounter sets and $n_{\rm enc}$ is the number of encounters per orbit.

The impulse approximation is based on the assumption that the time-scale of the encounter is much shorter than the orbital period of the perturbed body. To verify the validity of this assumption, we compare the period $P_{\rm PZ}(e=0)$ of the circular orbits with semimajor axes of $a_{\rm PZ}(e=0)$ with the time-scales of the encounters taken as $t_{\rm enc} = r_{\rm enc}/v_{\rm enc}$. The distributions of the ratio $P_{\rm PZ}(e=0)/t_{\rm enc}$ are shown in Fig. 6 by full lines. We found that for the vast majority of the encounters (more than 99 per cent), the ratio is higher than 100 and the assumption is well fulfilled. There is only a very small number of encounters (less than few dozen in the combined encounter sets, translating into $n_{\rm enc} \sim 2 \times 10^{-2}$ per orbit in Fig. 5), typically close ($r_{\rm enc} \lesssim 100$ au) and slow ($v_{\rm enc} \lesssim 10$ km s^{-1}), for which $P_{\rm PZ}(e=0)/t_{\rm enc} \lesssim 10$. Given that there is less than 1 per cent of encounters with $P_{\rm PZ}(e=0)/t_{\rm enc} < 50$, we neglect the inaccuracy of the impulse approximation for these cases.

The outer limit of the parking zone for higher eccentricities reaches smaller semimajor axes ($a_{\rm PZ}$ decreases with eccentricity) than for the circular orbits. The dotted lines in Fig. 6 show the distributions of the ratio $P_{\rm PZ}(e=0.99)/t_{\rm enc}$ for the three different orbits. Note that the distributions are shifted to lower values compared to $P_{\rm PZ}(e=0)/t_{\rm enc}$ (full lines). For an eccentricity of $e = 0.99$, we found that there is about 17 per cent of encounters with $P_{\rm PZ}(e=0.99)/t_{\rm enc} < 50$. The overall fraction of encounters with $P_{\rm PZ}(e=0.99)/t_{\rm enc} < 50$, however, is still relatively small, typically of the order of 10^{-4} out of the total number of encounters. More accurate approximations (Dybczynski 1994; Rickman et al. 2005) can be used to remedy this inaccuracy, but here we stick to the impulse approximation.

We determine the actual outer edge of the Solar system's parking zone such that the number of encounters along the orbit resulting in smaller $a_{\rm PZ}(e=0)$ is $n_{\rm enc} = 1$. These values are marked by the horizontal full grey line in Fig. 5. We obtain $a_{\rm PZ}(e=0) \approx 1280$, 940 and 690 au for the orbit with inwards migration, no migration and outwards migration, respectively. In Fig. 7, we show the resulting Solar system's parking zone. We list the parameters of the encounters used to calculate the outer edge of the parking zone in Table 3. These encounters were determined from the cumulative distribution of the number of encounters (Fig. 5) where we picked the encounters with the smallest $a_{\rm PZ}(e=0)$ of the first bin with $n_{\rm enc} > 1$. Note that these are example encounters and different combinations of parameters result in the same $a_{\rm PZ}(e=0)$ and parking zone's outer limit in the plane $e \times a$. For fixed semimajor axis a and eccentricity e, the parameters of the encounters resulting in the same change of impulse are bound as $M_{\rm enc}/[v_{\rm enc} r_{\rm enc}(r_{\rm enc} - a)] = {\rm const.}$ (equation 17). We use the following parameters to draw the outer edge of the Solar system's parking zone: $a = a_{\rm PZ}(e=0)$; $e = 0$; $M_{\rm enc}/[v_{\rm enc} r_{\rm enc}(r_{\rm enc} - a_{\rm PZ})] = 7.9$, 6.7 and $2.2 \times 10^{-5}\,{\rm M}_\odot\,{\rm au}^{-2}\,{\rm km}^{-1}\,{\rm s}$. The encounters with $M_{\rm enc}$, $v_{\rm enc}$ and $r_{\rm enc}$ that give these values will result in the same outer limit of the parking zone.

The solid black line in Fig. 7 corresponds to the original estimate made by Portegies Zwart & Jílková (2015) using the Scholz's star. The outer edge of the parking zone given by the encounters

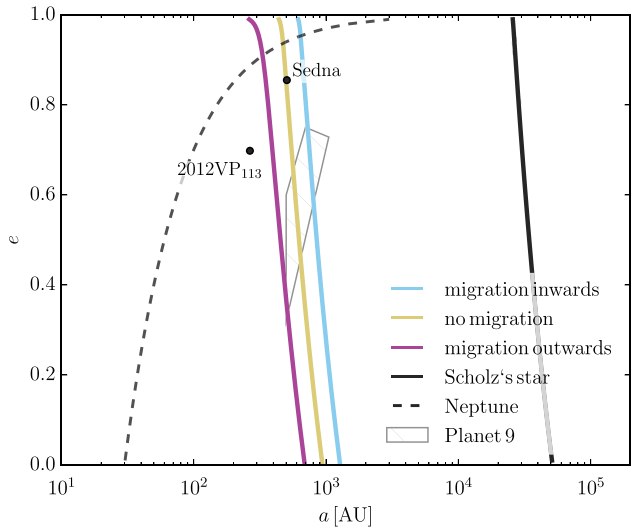

Figure 7. Solar system's parking zone in the plane of eccentricity e and semimajor axis a. Its inner limit is defined by the perturbations by Neptune and indicated by dashed black line. The blue, yellow and purple lines show its outer limit for solar orbits with different migration (see Fig. 2 and Table 3). The black line is the estimate of the outer limit using Scholz's star (Portegies Zwart & Jílková 2015). The two bullet points indicate the orbital elements of the inner Oort cloud bodies Sedna (Brown, Trujillo & Rabinowitz 2004) and 2012VP$_{113}$ (Trujillo & Sheppard 2014). The hashed triangle shows the orbital elements constrains for Planet 9 (Brown & Batygin 2016); see Section 5 for discussion.

Table 3. Stellar encounters used for the parking zone's outer limit in Fig. 7.

Orbit	$M_{\rm enc}$ ($M_\odot$)	$r_{\rm enc}$ (au)	$v_{\rm enc}$ (km s^{-1})
Migration inwards	0.11	1285	38.5
No migration	0.13	948	30.4
Migration outwards	0.43	721	21.4

derived here is located in the region corresponding to the inner Oort cloud, where objects like Sedna (Brown et al. 2004) and 2012VP$_{113}$ (Trujillo & Sheppard 2014) reside. The orbit migrating outwards from the denser inner regions of the Galaxy (violet line in Figs 2 and 7) results in the smallest parking zone. The orbit migrating inwards from the less dense outer regions (blue line in Figs 2 and 7) results in a parking zone that would not perturb the objects on Sedna-like orbits. This picture is consistent with Kaib et al. (2011) who concluded that the inner edge of the classical Oort cloud strongly depends on the orbit of the Sun, being smaller for the orbits that moved closer to the Galactic centre.

5 DISCUSSION

5.1 Effect of stellar encounters on the hypothetical P9

In order to explain some of the observed characteristics of distant KBOs or inner Oort cloud bodies, there has been ongoing discussion on an undiscovered planet in the outer Solar system (for example, Whitmire & Matese 1985; Matese & Whitmire 1986; Murray 1999; Horner & Evans 2002; Melita et al. 2004; Gomes, Matese & Lissauer 2006; Lykawka & Mukai 2008; Gomes, Soares & Brasser 2015 and others). The most recent prediction in this context was made by Batygin & Brown (2016) who showed that the presence of a distant planet – so-called P9 – can explain the observed orbital alignment of some KBOs and inner Oort cloud objects.

Brown & Batygin (2016) further constrained P9 to be of 5–20 $M_\oplus$ with an eccentricity of ∼0.2–0.8, semimajor axis of ∼500–1050 au (perihelion distance of ∼150–350 au) and inclination about 30°. The semimajor axes and eccentricities constrained for P9 are depicted in Fig. 7 and they overlap with the region of the outer edges of the Solar system's parking zone. This means that there was at least one encounter along the solar orbit that could have changed the aphelion velocity of P9 by 100 per cent. For such perturbation of P9, the encounter needs to have the appropriate geometry (where the encounter and P9's orbit are in the same plane). The outer limit of the parking zone serves as an estimate of the level to which a population of bodies orbiting in the Solar system was perturbed; that is, the concept of the parking zone assumes that there will be bodies on orbits with certain geometry with respect to the encounter plane. As a consequence, if a single body is orbiting at, or is close to the parking zone (such as P9), the probability of a perturbation occurring is given by the probability to obtain the appropriate geometry of the stellar encounter.

In this context, Li & Adams (2016) estimated the probability for the ejection of P9 from its current orbit by field stars. Using a large ensemble of simulations with Monte Carlo sampling, they first calculated the cross-section for the ejection and then integrated these along the solar orbit, assuming a constant number stellar density of 0.1 pc^{-3} and a velocity dispersion of 40 km s^{-1} for 4.6 Gyr. They estimate the probability of ejecting P9 due to a passing field star to be $\lesssim$3 per cent. Note that while Li & Adams (2016) considered an isotropic distribution of the direction of the encounters approach, Feng & Bailer-Jones (2014) find the distribution non-isotropic (encounters in the direction of the solar antapex are more common).

The existence of P9 is important to establish the existence of the parking zone of the Solar system. In Fig. 7, we show that the inner edge of the parking zone is delimited by Neptune's perturbing distance (dashed black line). If P9 really exists, the inner edge of the parking zone would be now delimited by its orbital parameters. This means that the inner edge of the parking zone would be shifted towards larger semimajor axes, at ∼10^3 au. In this case, the Solar system's parking zone would not exist.

5.2 Limitations in the computation of stellar encounters

We computed the Galactic stellar encounters in a more complete fashion than in Portegies Zwart & Jílková (2015). However, we note that our approach has limitations. First, we use different Galaxy models to compute the local stellar density and the velocity dispersion along the orbit of the Sun. This is inconsistent, because the local density and the stellar velocity dispersion might be different in the two Galaxy models used, even when these models might reproduce the observed properties of the Milky Way locally. Secondly, since we used only one snapshot from the N-body Galaxy model, the velocity dispersion along the orbit of the Sun does not evolve with time.

The estimate of the stellar encounters can be improved by computing in a consistent manner the local stellar density and the velocity dispersion along the orbit of the Sun. This can be achieved by using either the analytical or the N-body Galaxy model. In the analytical Galaxy model, the velocity dispersion can be derived by solving the Jeans equations. In this way, the temporal evolution of the velocity dispersion along the orbit of the Sun is also taken into account. However, several assumptions have to be made in order to obtain an uncomplicated solution for $v(t, x, y, z)$. For instance, it

is necessary to assume an initial velocity dispersion profile and the velocity ellipsoid aligned with the R- and z-axes. (Monari, Antoja & Helmi 2013, Section 2.3).

In the N-body Galaxy model, on the other hand, it is necessary to integrate the orbit of the Sun and to compute $\rho(t, x, y, z)$ and $\nu(t, x, y, z)$ using this model to make a consistent determination of $n_{\rm enc}$. To account for the temporal evolution of ρ and ν, such calculations must include enough snapshots obtained from the N-body simulation. This procedure, however, is not easy to execute given the complexity at handling the huge amount of data provided by each snapshot in the simulation.

The improvements mentioned above require further work and are outside the scope of this paper. The computation of the encounter probability by using either of the two methods is left for a future work.

6 SUMMARY AND CONCLUSIONS

We estimate the number of Galactic stellar encounters the Sun may have experienced in the past along its orbit through the Galaxy. We aim to improve the previous estimates of the outer edge of the Solar system's parking zone made by Portegies Zwart & Jílková (2015). The parking zone is the region in the plane of the eccentricity and semimajor axis where objects orbiting the Sun have been perturbed by stars belonging to the Sun's birth cluster but not by the planets or by Galactic perturbations. As a consequence, the orbits of objects located in the parking zone maintain a record of the interaction of the Solar system with the so-called solar siblings (Portegies Zwart 2009). These orbits carry information that can constrain the natal environment of the Sun.

We investigate the orbital history of the Sun by using an analytical potential containing a bar and spiral arms to model the Galaxy. In this potential, we integrate the orbit of the Sun back in time during 4.6 Gyr. Since we include the uncertainties in the present-day phase-space coordinates of the Sun, we obtain a collection of possible orbital histories. Here we study three different orbits, depending on the migration experienced by the Sun, namely: migration inwards, no migration and migration outwards. The Galactic stellar encounters are estimated for each of these orbits.

We compute the number of stellar encounters ($n_{\rm enc}$) by calculating the frequency of stellar passages experienced by the Sun along its orbit. This frequency is determined by computing the number density and the stellar velocity dispersion along the orbit of the Sun. We found that $n_{\rm enc} = 9.3 \times 10^4$, 28.2×10^4 and 17.5×10^4 for the orbits with inwards migration, outwards migration and no migration, respectively. We use these estimates to generate a sample of $n_{\rm enc}$ random stellar encounters with certain time of occurrence ($t_{\rm enc}$), mass ($M_{\rm enc}$), pericentre distance ($r_{\rm enc}$) and velocity ($v_{\rm enc}$). By looking at the distribution of stellar encounters in the space of $M_{\rm enc}$, $v_{\rm enc}$ and $r_{\rm enc}$, we found that most of the stellar encounters experienced by the Sun have been with low-mass stars ($M_{\rm enc} < 1$ M$_\odot$) with velocities of 20–100 km s^{-1}.

We calculate the outer edge of the Solar system's parking zone using the impulse approximation (Rickman 1976). For each solar orbit, we calculate the outer edge for 1000 different sets of encounters. The actual outer edge of the Solar system's parking zone is determined such that the number of encounters along the orbit resulting in smaller $a_{\rm PZ}(e)$ is $n_{\rm enc} = 1$. The parking zone is then located at about 250–700, 450–950 and 600–1300 au (Fig. 7) for the orbits with migration outwards, no migration and migration inwards, respectively.

Therefore, the orbital history of the Sun is important to establish the outer edge of the parking zone. From Fig. 7, it is also clear that the Sun has experienced stronger stellar encounters than those with the Scholz's star. As a consequence, the location of the outer edge of the parking zone is closer to the Sun than the previous estimates made by Portegies Zwart & Jílková (2015) and is comparable to the border between the inner and outer Oort cloud. Regardless of the migration of the solar orbit, we find that objects in the Solar system with semimajor axis smaller than about 200 au have not been perturbed by encounters with field stars. However, depending on the migration of the solar orbit, it is possible that the inner Oort cloud (including Sedna) has been perturbed.

We further discuss the effect of the stellar encounters on the stability of the orbit of a hypothetical P9. According to the orbital parameters of P9, this object is located in the same region as the outer edge of the parking zone. This means that there was at least one encounter along the solar orbit that could have changed the aphelion velocity of P9 by 100 per cent.

ACKNOWLEDGEMENTS

We thank Joris Hense and Inti Pelupessy for helpful discussions. We thank the reviewer for pointing out several drawbacks in our original methods and for comments that lead to substantial improvement of the presented work. This work was supported by the Nederlandse Onderzoekschool voor Astronomie (NOVA), the Netherlands Research Council NWO (grants #639.073.803 [VICI], #614.061.608 [AMUSE] and #612.071.305 [LGM]).

REFERENCES

Allen C. W., 1973, Astrophysical Quantities, 3rd ed. The Athlone Press
Allen C., Santillán A., 1991, Rev. Mex. Astron. Astrofis., 22, 255
Allen C., Moreno E., Pichardo B., 2006, ApJ, 652, 1150
Antoja T., Valenzuela O., Pichardo B., Moreno E., Figueras F., Fernández D., 2009, ApJ, 700, L78
Antoja T., Figueras F., Romero-Gómez M., Pichardo B., Valenzuela O., Moreno E., 2011, MNRAS, 418, 1423
Bailer-Jones C. A. L., 2015, A&A, 575, A35
Batygin K., Brown M. E., 2016, AJ, 151, 22
Bédorf J., Gaburov E., Fujii M. S., Nitadori K., Ishiyama T., Portegies Zwart S., 2014, Proceedings of the International Conference for High Performance Computing, Networking, Storage and Analysis, p. 54
Bellini A., Bedin L. R., Pichardo B., Moreno E., Allen C., Piotto G., Anderson J., 2010, A&A, 513, A51
Brown M. E., Batygin K., 2016, ApJ, 824, L23
Brown M. E., Trujillo C., Rabinowitz D., 2004, ApJ, 617, 645
Brunini A., Fernandez J. A., 1996, A&A, 308, 988
Cox D. P., Gómez G. C., 2002, ApJS, 142, 261
Dones L., Brasser R., Kaib N., Rickman H., 2015, Space Sci. Rev., 197, 191
Drimmel R., 2000, A&A, 358, L13
Dybczynski P. A., 1994, Celest. Mech. Dyn. Astron., 58, 139
Dybczyński P. A., Berski F., 2015, MNRAS, 449, 2459
Feng F., Bailer-Jones C. A. L., 2014, MNRAS, 442, 3653
Feng F., Bailer-Jones C. A. L., 2015, MNRAS, 454, 3267
Ferrers N. M., 1877, Pure Appl. Math., 14, 1
Fouchard M., Froeschlé C., Rickman H., Valsecchi G. B., 2011, Icarus, 214, 334
García-Sánchez J., Weissman P. R., Preston R. A., Jones D. L., Lestrade J.-F., Latham D. W., Stefanik R. P., Paredes J. M., 2001, A&A, 379, 634
Gerhard O., 2011, Mem. Soc. Astron. Ital. Suppl., 18, 185
Gomes R. S., Matese J. J., Lissauer J. J., 2006, Icarus, 184, 589
Gomes R. S., Soares J. S., Brasser R., 2015, Icarus, 258, 37
Heisler J., Tremaine S., 1986, Icarus, 65, 13
Holmberg J., Nordström B., Andersen J., 2009, A&A, 501, 941

Horner J., Evans N. W., 2002, MNRAS, 335, 641
Hut P., Tremaine S., 1985, AJ, 90, 1548
Jakubík M., Neslušan L., 2008, Contrib. Astron. Obs. Skalnate Pleso, 38, 33
Jakubík M., Neslušan L., 2009, Contrib. Astron. Obs. Skalnate Pleso, 39, 85
Jílková L., Carraro G., Jungwiert B., Minchev I., 2012, A&A, 541, A64
Jílková L., Portegies Zwart S., Pijloo T., Hammer M., 2015, MNRAS, 453, 3157
Jurić M. et al., 2008, ApJ, 673, 864
Kaib N. A., Roškar R., Quinn T., 2011, Icarus, 215, 491
Kepler S. O., Kleinman S. J., Nitta A., Koester D., Castanheira B. G., Giovannini O., Costa A. F. M., Althaus L., 2007, MNRAS, 375, 1315
Kroupa P., 2001, MNRAS, 322, 231
Li G., Adams F. C., 2016, ApJ, 823, L3
Lykawka P. S., Mukai T., 2008, AJ, 135, 1161
Mamajek E. E., Barenfeld S. A., Ivanov V. D., Kniazev A. Y., Väisänen P., Beletsky Y., Boffin H. M. J., 2015, ApJ, 800, L17
Mamajek E. E., 2016, preprint (arXiv:e-prints)
Martínez-Barbosa C. A., Brown A. G. A., Portegies Zwart S., 2015, MNRAS, 446, 823
Matese J. J., Whitmire D. P., 1986, Icarus, 65, 37
Melita M. D., Williams I. P., Collander-Brown S. J., Fitzsimmons A., 2004, Icarus, 171, 516
Minchev I., Famaey B., 2010, ApJ, 722, 112
Minchev I., Chiappini C., Martig M., 2013, A&A, 558, A9
Miyamoto M., Nagai R., 1975, PASJ, 27, 533
Monari G., Antoja T., Helmi A., 2013, preprint (arXiv:1306.2632)
Monari G., Helmi A., Antoja T., Steinmetz M., 2014, A&A, 569, A69
Murray J. B., 1999, MNRAS, 309, 31
Nordström B. et al., 2004, A&A, 418, 989
Oort J. H., 1950, Bull. Astron. Inst. Neth., 11, 91
Pecaut M. J., Mamajek E. E., 2013, ApJS, 208, 9
Pecaut M. J., Mamajek E. E., Bubar E. J., 2012, ApJ, 746, 154
Pelupessy F. I., van Elteren A., de Vries N., McMillan S. L. W., Drost N., Portegies Zwart S. F., 2013, A&A, 557, A84
Plummer H. C., 1911, MNRAS, 71, 460
Portegies Zwart S. F., 2009, ApJ, 696, L13
Portegies Zwart S. F., Jílková L., 2015, MNRAS, 451, 144
Portegies Zwart S., McMillan S. L. W., van Elteren E., Pelupessy I., de Vries N., 2013, Comput. Phys. Commun., 183, 456
Rickman H., 1976, Bull. Astron. Inst. Czech., 27, 92
Rickman H., 2014, Meteorit. Planet. Sci., 49, 8
Rickman H., Fouchard M., Valsecchi G. B., Froeschlé C., 2005, Earth Moon Planets, 97, 411
Rickman H., Fouchard M., Froeschlé C., Valsecchi G. B., 2008, Celest. Mech. Dyn. Astron., 102, 111
Romero-Gómez M., Athanassoula E., Antoja T., Figueras F., 2011, MNRAS, 418, 1176
Roškar R., Debattista V. P., Quinn T. R., Stinson G. S., Wadsley J., 2008, ApJ, 684, L79
Schönrich R., Binney J., Dehnen W., 2010, MNRAS, 403, 1829
Sellwood J. A., Binney J. J., 2002, MNRAS, 336, 785
Trujillo C. A., Sheppard S. S., 2014, Nature, 507, 471
Whitmire D. P., Matese J. J., 1985, Nature, 313, 36
Wielen R., Fuchs B., Dettbarn C., 1996, A&A, 314, 438

This paper has been typeset from a TEX/LATEX file prepared by the author.